Study of magnetic particles pulse-injected into an annular SPLITT-like channel inside a quadrupole magnetic field

Mauricio Hoyos[a,b], Lee R. Moore[b], Kara E. McCloskey[b,c], Shlomo Margel[d], Merav Zuberi[d], Jeffrey J. Chalmers[c], Maciej Zborowski[b,*]

[a]*Ecole Supérieure de Physique et Chimie Industrielles, Laboratoire de Physique et Mécanique des Milieux Hétérogènes, UMR 7636 CNRS, Paris, France*
[b]*The Cleveland Clinic Foundation, Department of Biomedical Engineering, 9500 Euclid Avenue, Cleveland, OH 44195, USA*
[c]*The Ohio State University, Department of Chemical Engineering, 121 Koffolt Laboratories, 140 West 19th Avenue, Columbus, OH 43210-1180, USA*
[d]*Bar-Ilan University, Department of Chemistry, 52900 Ramat-Gan, Israel*

Abstract

Advantages of the continuous magnetic flow sorting for biomedical applications over current, batch-wise magnetic separations include high throughput and a potential for scale-up operations. A continuous magnetic sorting process has been developed based on the quadrupole magnetic field centered on an annular flow channel. The performance of the sorter has been described using the conceptual framework of split-flow thin (SPLITT) fractionation, a derivative of field-flow fractionation (FFF). To eliminate the variability inherent in working with a heterogenous cell population, we developed a set of monodisperse magnetic microspheres of a characteristic magnetization, and a magnetophoretic mobility, similar to those of the cells labeled with a magnetic colloid. The theory of the magnetic sorting process has been tested by injecting a suspension of the magnetic beads into the carrier fluid flowing through the sorter and by comparing the theoretical and experimental recovery versus total flow-rate profiles. The position of the recovery maxima along the total flow-rate axis was a function of the average bead magnetophoretic mobility and the magnetic field intensity. The theory has correctly predicted the position of the peak maxima on the total flow-rate axis and the dependence on the bead mobility and the field intensity, but has not correctly predicted the peak heights. The differences between the calculated and the measured peak heights were a function of the total flow-rate through the system, indicating a fluid-mechanical origin of the deviations from the theory (such as expected of the lift force effects in the system). The well-controlled elution studies using the monodisperse magnetic beads, and the SPLITT theory, provided us with a firm basis for the future sorter evaluation using cell mixtures. © 2000 Elsevier Science B.V. All rights reserved.

Keywords: Split-flow thin fractionation; Field-flow fractionation; Monodisperse microspheres; Magnetic beads; Pulse-injection; Magnetic separation; Quadrupole field

1. Introduction

Split-flow thin (SPLITT) fractionation is a continuous, preparative-scale separation technique for

*Corresponding author. Tel.: +1-216-445-9330; fax: +1-216-444-9198.

E-mail address: zborow@bme.ri.ccf.org (M. Zborowski).

the binary separation of colloids, macromolecules and particulate materials [1]. It has been derived from field-flow fractionation (FFF) by Giddings to extend the capabilities of FFF which are limited to analytical separations of high molecular mass and particulate analytes [2]. The SPLITT separator consists of a ribbon-like channel, with two inlets, labeled a′ and b′, and two outlets, labeled a and b, exposed to an external force field as in a Hele Shaw cell [3]. Typically, centrifugal or electric fields are used [4–6]. The sample feed containing a mixture of the analytes, and a carrier fluid are injected at inlet ports a′ and b′, respectively, and the depleted and the enriched fractions are collected at outlet ports a and b, respectively, in a continuous manner, Fig. 1. The separation is achieved by a differential migration of analytes across the flow streamlines when exposed to the external force field. An ideal binary separation occurs when each compound elutes separately from the two different outlets. In addition to the primary forces driving the separation, such as centrifugal or electrical, there may be contributions from the diffusion and the secondary forces, such as lift forces, to the overall separation effect [7]. The theory of SPLITT fractionation in rectangular flow channels exposed to homogenous force fields is well developed [1,7]. It has been tested experimentally in application to separation of red blood cells from whole blood solutions [4,8]. The nature of the field determines the particle parameters which can be used for the separation, for instance the gravitational (and centrifugal) field separates particles according to their sedimentation velocity (a function of the particle size and density), and the electric field separates particles according to their dielectric constant (and size) [5,6].

We have proposed to extend the SPLITT approach to flows in annular flow channels and axisymmetric, constant force fields [9–11]. The advantages of such novel flow and field configuration is the absence of the side-wall effects, with the potential of an increased resolving power of the separation, and a wider choice of the available force fields (including the magnetic field). The theory of SPLITT separation in an annular flow and a quadrupole magnetic field has been developed [11,12]. The main goal of this
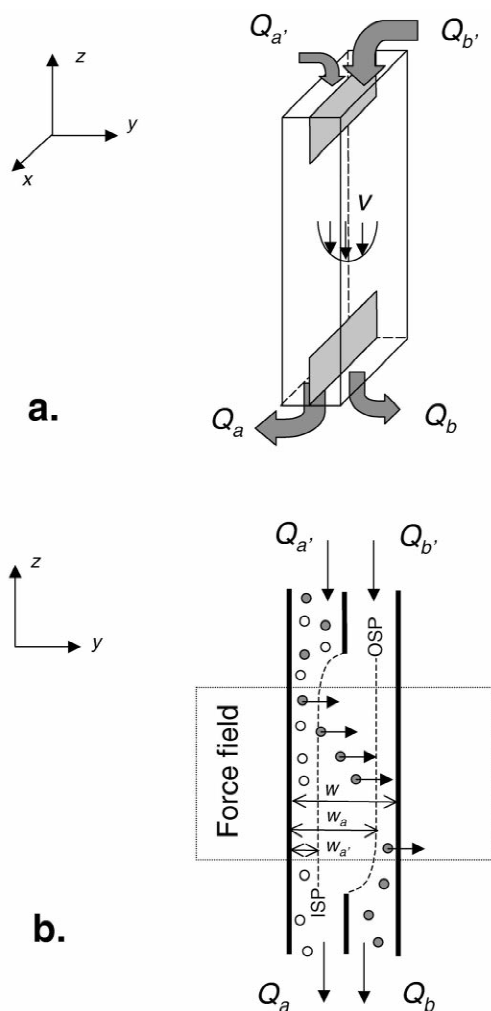

Fig. 1. The original split flow-thin (SPLITT) fractionator channel as proposed by Giddings (adapted from Refs. [1,2]). (a) A three-dimensional representation of the channel with the inlet and outlet flow-rates indicated by arrows (the size of the arrows indicate differences in the volumetric flow-rates). (b) A longitudinal section of the channel with inlet and outlet splitting planes, ISP and OSP, respectively, represented by dashed lines; the splitting plane positions are dictated by the relative values of the inlet and outlet flow-rates. The separation is achieved by the target particles (gray circles) migration across the transport lamina (demarcated by ISP and OSP) induced by the external force field.

paper is to compare the prediction of the theory with experiment in which we have used pulse injections of monodisperse magnetic particles of known mag-

netophoretic mobilities, in well-controlled magnetic field and fluid flow conditions. The magnetic quadrupole field was generated by an assembly of specially-designed pole pieces and permanent magnets.

The quadrupole magnetic SPLITT (QMS) fractionator was operated in the transport mode, analogous, in effect, to the time-of-flight operation of the mass spectrometer [13]. In the transport mode, a steady state is achieved in which particles within a narrow range of the magnetophoretic mobilities, defined by the operating conditions of the QMS, appear in a purified form at outlet b. The particles outside the mobility range either strike the wall and stay inside the channel for the duration of the experiment (high mobility limit) or never make it across the flow streamlines and are eluted at the outlet a (low mobility limit). Therefore, only those particles whose residence time (or the "time-of-flight") inside the QMS separator matches the time necessary to reach outlet b are selected in outlet b. The transport mode of separation is strongly dependent on the selection of the operating conditions, such as the magnitude of the force field, and the total and the fractional flow-rates. The QMS theory allows for prediction of the particle recovery in outlets a and b as a function of its mobility and other system parameters. The focus of this paper is to test the theoretical predictions using two different magnetic force fields, and a range of the total flow-rates, for set values of the fractional flow-rates. We envisage the potential, future applications of the SPLITT-like, QMS separation to rapid, high-volume cell sorting [10,14]. However, in this study we used monodispersed magnetic polymeric particles to eliminate cell heterogeneity as a source of the variability in the system.

In order to expedite the experimental investigations, we used a pulse-injection technique, common in chromatography and in FFF separations. The pulse-injection approach allowed us to perform a large number of experiments in a relatively short time, using a minimum amount of the magnetic reference beads. The elution profiles from outlets a and b of the QMS channel following pulse injection were analyzed using chromatographic peak deconvolution techniques in order to find the peak area. This approach allowed us to analyze the QMS separation process for a wide range of experimental parameters.

2. Materials and methods

2.1. Theory

2.1.1. Particle–fluid interaction

The theory of the continuous SPLITT fractionation for rectangular flow channels in homogenous force fields has been formulated by Williams et al. [15]. The characteristic feature of the theory is the concept of the inlet and outlet splitting planes, ISP and OSP, which describe imaginary flow streamplanes originating and ending at the edges of the inlet and outlet flow splitters, respectively, Fig. 1. For low aspect-ratio (height, w, to width) rectangular flow channels for which the flow profile is parabolic over a large portion of the channel width, the ISP and OSP positions, $w_{a'}$ and w_a, can be determined analytically from the known fractional flow-rates at the channel inlet and outlet, $Q_{a'}/Q$ and Q_a/Q, respectively:

$$\frac{Q_{a'}}{Q} = 3 \cdot \left(\frac{w_{a'}}{w}\right)^2 - 2 \cdot \left(\frac{w_{a'}}{w}\right)^3 \qquad (1)$$

There is a similar expression linking Q_a/Q and w_a (Fig. 1a). Another important and useful concept in the SPLITT theory is that of the transport lamina, which is the volume of the flowing solution enclosed by the ISP and the OSP. It represents a "resistive element" to the transport processes inside the SPLITT channel, and as such has been referred to as a "virtual membrane" [8,15]. The transport lamina thickness is given by the absolute value of the ISP and OSP distance interval, $w_a - w_{a'}$, Fig. 1b.

The SPLITT theory for annular channels leads to more complex relationships between the ISP and OSP (renamed inlet splitting cylinder, ISC, and outlet splitting cylinder, OSC, correspondingly), and the fractional inlet and outlet flow-rates, than those for the rectangular channel. The annular flow channel is formed by two concentric cylinders, equipped with two concentric inlet and outlet flow splitters, Fig. 2. The channel is exposed to a coaxial, radial force field, such as is produced by a quadrupole magnetic field acting on magnetic dipoles [9,12]. Typically,

Fig. 2. The annular SPLITT-like channel proposed for use in combination with the quadrupole magnetic field [9–11]. (a) A three-dimensional representation of the channel with the central portion consisting of a solid rod. (b) A longitudinal section of the channel showing various system parameters as defined in the text. In particular, note particle trajectories related to the cut-off mobilities m_0 and m_3. The part exposed to the external magnetic force field, with the well-defined, constant ISC and OSC radii, comprises the QMS separation element.

the mixture of magnetic and non-magnetic particles is injected at the inlet port a′, and the carrier fluid is delivered to the inlet port b′. For an ideally operating system, the magnetic particles migrate radially towards the outer wall during their convective transport down the channel, and are eluted at the outlet b,

whereas the non-magnetic particles stay with their streamlines and are swept to outlet a, Fig. 2, resulting in separation of the magnetic from non-magnetic species.

The laminar flow velocity profile in an annular channel is given by:

$$v(\rho) = 2\frac{\langle v \rangle}{A_1} \cdot (1 - \rho^2 - A_2 \ln \rho) \qquad (2)$$

where $\rho = r/r_o$, and r_o is the radius of the inner wall of the outer cylinder, $\langle v \rangle$ is the mean flow velocity, related to the total flow-rate, $Q = \langle v \rangle \pi r_0^2 \cdot (1 - \rho_i^2)$, where $\rho_i = r_i/r_o$ and r_i is the radius of the inner rod, Fig. 2. The parameters $A_2 = (1 - \rho_i^2)/\ln \rho_i$ and $A_1 = 1 + \rho_i^2 + A_2$ are characteristic constants of the annular channel geometry. The relative positions of the ISC and OSC, ρ_{ISC} and ρ_{OSC}, respectively, were obtained numerically by solving the integral:

$$Q_{a'} = \frac{4\pi r_0^2 \langle v \rangle}{A_1} \int_{\rho_i}^{\rho_{ISC}} (1 - \rho^2 - A_2 \ln \rho)\rho \, d\rho \qquad (3)$$

A similar integral exists linking Q_a and ρ_{OSC}. The theoretical model allowed us to predict the particle trajectories for any radial force field. For a given channel geometry and force field, the particle trajectories were determined by their initial radial positions at the entry into the magnetic field, ρ_1, the particle magnetophoretic mobility (see below), m, the flow velocity profile, Eq. (2), and the local force field strength, S_m, defined below (Eq. (14)). The particle trajectories were obtained by solving two simultaneous differential equations for the axial and radial velocities:

$$\begin{cases} \dfrac{dz}{dt} = v(\rho) \\[2mm] r_0 \dfrac{d\rho}{dt} = u_m(\rho) \end{cases} \qquad (4)$$

with the initial conditions:

$$\begin{cases} z(0) = 0 \\ \rho(0) = \rho_1, \quad \rho_i < \rho_1 < \rho_{ISC}, \quad 0 < t < t_f \end{cases} \qquad (5)$$

where u_m is the magnetically-induced particle radial velocity, ρ_{ISC} is the relative radial position of the ISC (Fig. 2), and t_f is the particle time-of-flight. The particle time-of-flight was determined from the final particle position inside the channel: [$z(t_f) = L$ and $\rho_i < \rho(t_f) < 1$] or [$0 < z(t_f) < L$ and $1 = \rho(t_f)$].

Depending on their final positions, the particles were assigned to channel outlets using the following decision-making algorithm:

$$\begin{cases} \rho(t_f) < \rho_{OSC} & \text{outlet a} \\ \rho_{OSC} \le \rho(t_f) < 1 & \text{outlet b} \\ 1 = \rho(t_f) & \text{wall} \end{cases} \qquad (6)$$

where "wall" designates the particle fraction retarded on the inner wall of the outer cylinder. By eliminating the time variable in Eq. (4), the trajectory $\rho = \rho(z)$ was determined by solving the integral:

$$\int_0^z dz = \int_{\rho_1}^{\rho} \frac{v(\rho)}{u_m(\rho)} r_0 \, d\rho$$

$$= \frac{2\langle v \rangle r_0}{A_1} \int_{\rho_1}^{\rho} \frac{(1 - \rho^2 - A_2 \ln \rho)}{m S_m} \, d\rho \qquad (7)$$

where the magnetically-induced radial velocity, u_m, was substituted by the product of the particle magnetophoretic mobility, m, and the force field strength, S_m, as described in the next section. The axial length, L, the length of the force field, was taken to be equal to the length of the magnet. Additional details of the theory are given elsewhere [11,12]. A computer algorithm was developed to calculate a large number of particle trajectories over a number of initial particle positions, and a number of different particle mobilities, approximating the continuous distribution of those two parameters. Theoretical recovery as a function of total flow-rate data was calculated with a Maple V (Waterloo Maple, Ontario, Canada) computer program run on an IBM-compatible personal computer. The program read in paired mobility–frequency increment data obtained from cell tracking velocimetry (CTV, see next section). From each data set's mobility value, two trajectories are assigned: one beginning at ($z = 0$, $\rho = \rho_i$) and the other beginning at ($z = 0$, $\rho = \rho_{ISC}$). These initial positions bound the feed streamlines as they enter the region of the magnetic force, the QMS separation element. The terminal radii of these trajectories, at $z = L$, were calculated. A series of conditional statements enabled the calculation of the single data pair's fractional recoveries at outlets a, b or the wall, w, determined by the location of the terminal radii with respect to $\rho = \rho_{OSC}$ and $\rho = 1$. These recoveries were calculated using external subroutines. Each recovery was then weighted by the corresponding mobility frequency. The process is repeated for all the data

pairs, while the weighted recoveries are summed, yielding the overall recoveries in outlet a, b, and the wall, w, for the choice of experimental conditions and magnetic particles. The theoretical model rested on the following assumptions: point-like particles; no inter-particle interactions; perfect field and flow geometry; magnetic and viscous forces only; and no fringing fields at the ends of the QMS separation element. The resulting distribution of the particle numbers between the outlets a and b (and the wall, w) provided a theoretical result of the QMS separation simulation, accessible to experimental verification.

2.1.2. Particle–field interaction

The magnetic body force, f_m, also called the Kelvin magnetization force density, acting on a freely-suspended induced magnetic dipole is given by the following expression:

$$f_m = \chi \left| \nabla \left(\frac{B^2}{2\mu_0} \right) \right| \tag{8}$$

where the straight brackets, $|\cdot|$, denote the magnitude of a vector, B is the magnetic induction (or magnetic flux density), μ_0 is the magnetic permeability of vacuum, and $\nabla = [\partial/\partial x, \partial/\partial y, \partial/\partial z]$ is a nabla (or del) operator, producing a gradient when operating on a scalar quantity. The magnetic volumetric susceptibility of the dipole material, χ, is given by:

$$\chi = \frac{M}{H} \tag{9}$$

where M is the magnetization of the dipole material in an external field of strength H. For paramagnetic materials, $\chi = $ constant. For ferromagnetic materials, such as those used for synthesis of the reference magnetic beads, the magnetization, M, reaches a plateau with increasing H, with the corresponding saturation magnetization $M_s = $ constant. In such cases, the magnetic body force reduces to:

$$f_m = \frac{M_s}{H} \left| \nabla \left(\frac{B^2}{2\mu_0} \right) \right| = M_s |\nabla B| \tag{10}$$

where the use was made in the last equation of the relationship $B = \mu_0 H$, which holds true for non-magnetic media, such as aqueous solutions of physiological electrolytes. For quadrupole fields:

$$B = B_0 \rho \tag{11}$$

where B_0 is the magnetic field at the inner wall of the outer cylinder (at $\rho = 1$). By substituting Eq. (11) into Eqs. (10) and (8) we obtain the following two expressions for the magnetic body force:

$$f_m = \begin{cases} \chi \cdot \dfrac{B_0^2}{\mu_0 r_0} \cdot \rho & \text{paramagnetic particles} \\[2mm] \dfrac{M_s B_0}{r_0} & \text{ferromagnetic particles} \end{cases} \tag{12}$$

Note that the body force acts differently on paramagnetic and ferromagnetic particles in the quadrupole field: it increases with radial distance for the paramagnetic particles, and stays constant for the ferromagnetic particles. Both models of the magnetic body force were used in the computational simulation of the separation process.

In analogy to the term ''electrophoretic mobility'' describing the motion of electrically charged species in a viscous medium exposed to external electrical field, we adapted the term ''magnetophoretic mobility'' to describe the motion of magnetic particles in the aqueous media exposed to the magnetic field [16–18]. The particle velocity in the external magnetic field, u_m:

$$u_m = m S_m \tag{13}$$

is the product of the particle mobility, m, and the local force field strength, S_m, defined as:

$$S_m = \left| \nabla \left(\frac{B^2}{2\mu_0} \right) \right| \tag{14}$$

The magnetophoretic mobilities, m, of the reference magnetic beads used in this study were measured using CTV [17,18]. The CTV technique allows for an automated motion analysis of a large number (hundreds to thousands) of μm-sized particles exposed to external force fields, in the field of view of a microscope. The unique feature of the CTV instrument developed in our laboratories is that $S_m = $ constant, which significantly improves the resolution and the accuracy of the method [17,18]. The CTV output provided us with the statistics of the magnetic bead samples, including mobility frequency histograms, average mobilities and the standard deviations, Fig. 4. The experimentally-measured distribu-

tion of the magnetophoretic mobilities was fed into the computer program calculating the magnetic particle trajectories in the QMS separator, and was used to calculate the predicted distribution of the magnetic particles between outlets a and b of the QMS separator, as outlined in the previous section.

2.2. Experiment

The present study was motivated by potential applications of the QMS technique to continuous separation of magnetically-labeled cells [10,12,14]. The QMS technique relies on the transport mode of separation (as opposed to the equilibrium mode of separation), and therefore is sensitive to the flow-rates through the system. The combined theoretical and experimental analysis of the QMS separation process allowed us to study the effect of flow-rates on the fractional retrieval and enrichment of particle populations as a function of their magnetophoretic mobility. Such studies will become important for the future development of efficient cell separation protocols based on the cell surface marker expression [14].

In principle, the SPLITT-like fractionation is well adapted to binary separations but requires careful flow-rate adjustments for polydisperse sample separation, such as cell mixtures. In order to eliminate the effects of sample heterogeneity, we selected a model system of monodisperse magnetic particles in this study. The size and magnetic characteristics of the particles (their magnetophoretic mobility) were selected so that they resembled the characteristic of the cells labeled with magnetic colloids [18]. The particle concentration was chosen so as to minimize particle–particle interactions (the particle volume concentration was well below 1%). Although the potential, future QMS sorter applications may require a continuous mode of operation, we selected the pulse-injection mode for the sorter evaluation because of its economical use of time and resources. The lack of inter-particle interactions expected at a low particle concentration assured us that the pulse-injection results are also relevant to the continuous sorter operation. The pulse-injection approach is well accepted in studies on the behavior of separation systems, such as FFF.

2.2.1. Determination of retrieval factors F_a and F_b by pulse injections

The distribution of magnetic particles between outlets a and b was characterized experimentally by the retrieval factors, F_a and F_b, respectively. The retrieval factor, F_b, of an analyte at outlet b of the separator was defined as the ratio of the number of the analyte particles eluted at the outlet b, N_b, to the number of the analyte particles injected into the system, N:

$$F_b = \frac{N_b}{N} \tag{15}$$

A similar formula was obtained for the retrieval factor at the outlet a, F_a. The retrieval factor is a measure of the yield, or the fractional recovery, of the analyte. In our past studies on bead and cell sorting we have used automated particle counters and analytical balances to determine the volume fraction of the cells, and beads. Due to the use of the syringe pumps and the closed fluid flow pathway through the QMS separator (see below), such determination of the retrieval factors was possible only at the end of the sorting run, once per run, which significantly limited the amount of data per run [10].

In order to improve the speed of the data acquisition, and to reduce costs involved in the use of relatively large amounts of magnetic beads necessary for particle counting, we adopted an on-line particle detection method, typical of analytical chromatography. We attached two 245 nm UV detectors with 32-μl flow cells (VUV-10; HyperQuan, Colorado Springs, CO, USA) to the outlets a and b of the QMS separator, Fig. 3. The detector signal was fed into an analog-to-digital converter (DI-190, Dataq Instruments, Akron, OH, USA) and stored in an IBM-compatible personal computer. The data were analyzed using a statistical software package (WinDaq Lite, Dataq Instruments) which included specialized software for peak deconvolution and parameterization (PeakFit; SPSS, Chicago, IL, USA). The pulse of a small volume of the particle suspension applied to the inlet of the QMS separator (at the inlet a′) produced two pulses of increased light attenuation at the outlets a and b, characteristic of the distribution of the eluted fractions between outlets a and b, respectively. The changes in the light attenuation due
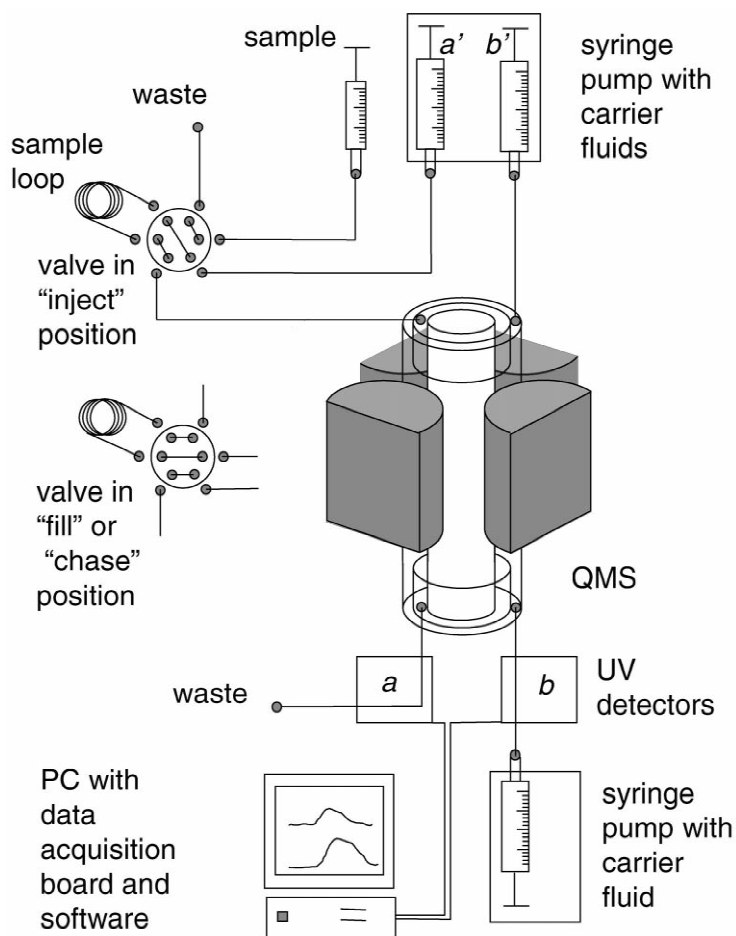
Fig. 3. Schematic representation of the experimental set-up components.

to the passage of the particle pulse through the detector were correlated with the number of the particles in the pulse, for different particle concentrations, and different flow-rates, as described below. The correlation of the light attenuation peaks with the volume fractions of particles passing through the UV detector led to an accurate and direct determination of the retrieval factors. Generally, the UV detectors are used mostly in pulse-injection studies but could also be used in the continuous mode of operation. In our hands, the pulse-injection technique was rapid and allowed us to perform a large number of injections for different total and fractional flow-rates, thus significantly increasing the amount of data collected during a single run. It was

also less expensive, because significantly smaller sample volumes were required than those needed for particle counting.

2.2.2. Calibration of the particle elution curve

For monodisperse, dilute particle suspensions the light attenuation due to scattering is directly proportional to the concentration of the particles in suspension, c:

$$A = kc \tag{16}$$

where k is a constant independent of concentration, but dependent on light wavelength, and instrument

and particle parameters [19], and c is the particle number concentration:

$$c = \frac{n}{V} \qquad (17)$$

where V is the volume. For definiteness, the following derivation will apply to the outlet b detector. Its extension to outlet a is straightforward by a suitable substitution of subscript b by subscript a (see also Fig. 3). As the pulse of the particle suspension flows through the UV detector, the absorbance A changes from the baseline (no particles in the detector chamber) to a maximum and back to the baseline. The area, h_b, under the elution curve $A = A(t)$, recorded over the time interval of the particle elution from the QMS separator, $t_1 - t_0$, is a measure of the total number of the particles, N_b, passing through the detector b during that time interval:

$$h_b = \sum_{t_0}^{t_1} A(t)\Delta t = k \sum_{t_0}^{t_1} c(t)\Delta t = \frac{k}{V}\sum_{t_0}^{t_1} n(t)\Delta t$$
$$= \frac{k\Delta t}{V}\sum_{t_0}^{t_1} n(t) = \frac{kN_b}{Q_b} \qquad (18)$$

where V is the volume of the particle suspension passing the detector b chamber in time interval Δt, and $Q_b = V/\Delta t$ is the volumetric flow-rate through the detector b chamber. The selection of the parameter Δt depended on the time response of the detector, and it was less than 0.01 of the total time $t_1 - t_0$. The time points t_0 and t_1 were determined by inspection of the absorbency curves in the usual manner, by a single operator (t_0 corresponded to the rise of A from its baseline value, t_1 corresponded to the return to the baseline value). The summation was carried out using the peak analysis software. By substituting the expression for N_b from Eq. (18) to the definition of the retrieval factor, Eq. (15), one obtains:

$$F_b = \frac{Q_b h_b}{Qh} \qquad (19)$$

where the subscripted quantities correspond to the normal operation mode of the QMS separator (both a and b outlets open), and the un-subscripted quantities correspond to the reference operation mode, in which the entire sample flow is directed into the detector b (the outlet a is blocked off), with the flow channel placed outside the magnetic field. A similar expres-

sion was obtained for the detector a. The reference h values were determined separately for each detector at a single total flow-rate. In principle:

$$F_a + F_b + F_w = 1 \qquad (20)$$

where F_w is the particle fraction retarded on the accumulation wall. The fraction F_w was calculated as a difference between $F_a + F_b$ and the unity. The pulse injection volume was 50 µl, the particle number concentration was approximately $5 \cdot 10^8$/ml. Each pulse injection was performed in duplicate. An example of typical elution profiles from the outlets a and b of the QMS separator are shown in Fig. 5.

2.2.3. Magnetic reference beads

The separation experiments were performed on monodisperse magnetic microspheres synthesized in the laboratory of one of the authors (S.M.). The organic–inorganic hybrid microspheres of narrow size distribution (mean diameter of 2.70 µm±0.04 µm SD), consisted of polystyrene core, a shell of magnetite/hematite (Fe_3O_4), and coated by an outer shell of 30 to 40 nm silica nanospheres to stabilize the metal shell. The amount of the iron compound, and thus the magnetization of the microspheres, was controlled by seeded polymerization of iron salts on the polystyrene core particles, followed by seeded polymerization of the protective silica coat [$Si(OEt)_4$], as published elsewhere [20]. The magnetic microspheres were dried in the vacuum oven, and their magnetization measured as a function of the applied magnetic field strength in the vibrating sample magnetometer (VSM, Oxford Instruments, Oxfordshire, UK). Three sets of the magnetic microspheres were selected for this study, of different saturation magnetization as shown in Table 1. The magnetophoretic mobility of the magnetic microspheres was measured using a CTV instrument set up in the laboratory of one of us (J.J.C.), according to procedures published elsewhere [18]. Briefly, the particles were suspended in distilled water containing 0.05% Triton X-100 (Sigma–Aldrich, St. Louis, MO, USA), and the single particle suspension was obtained by sonication. The particle number concentration was adjusted to approximately $5 \cdot 10^8$/ml. The velocity of the particles in solution was measured in the external magnetic field, generating the force field strength of $S_m = 198$ T A/mm^2, which

Table 1
The monodisperse magnetic microspheres[a]

Type	Density (g/cm^3)	M_s (A/m) at $H = 1.06 \cdot 10^6$ A/m	$\chi \cdot 10^3$	$m \cdot 10^4$ (mm^3/T A s)
A	1.129±0.031	3100±1700	2.9±1.6	9.2±5.1
B	1.113±0.026	460±310	4.30±0.29	1.06±0.70
C	1.106±0.024	290±270	2.68±0.25	0.31±0.27

[a] Hybrid microspheres of diameter 2.7 μm±1.5% (RSD) consisting of a polystyrene core, magnetite/hematite shell (Fe$_3$O$_4$), and coated by a silica shell of silica nanospheres 30 to 40 nm diameter [20]. All values are listed as mean±1 SD.

was nearly constant for the entire field of observation (5× objective). The images of the moving particles were acquired by a CCD camera mounted on the microscope (CCD 4915; Cohu, San Diego, CA, USA) and analyzed by the CTV software running on a IBM-compatible personal computer with the image board (μ-Tech Vision 1000 PCI Bus Frame Grabber; MuTech, Billerica, MA, USA). Typically, the motion of several hundred microspheres of a given type were analyzed, and displayed in the form of the magnetophoretic mobility histograms. The mobility histograms of the three sets of particles selected for this study are shown in Fig. 4. Their mean mobilities are shown in Table 1.
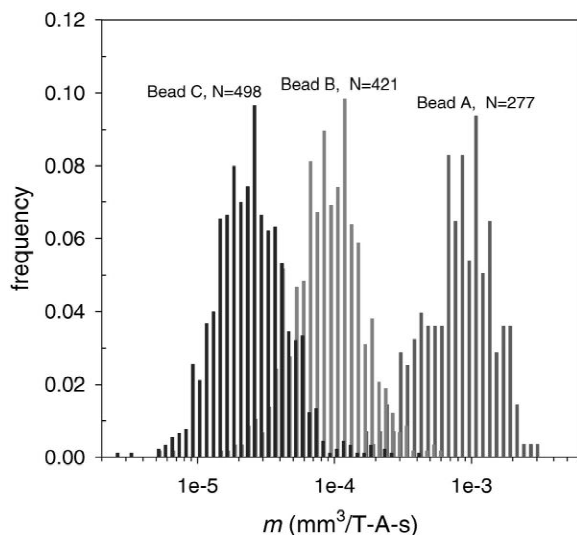

Fig. 4. The magnetophoretic mobility distributions, m, of three types of the monodisperse magnetic beads used in this study (A, B and C) as measured by the cell tracking velocimetry (CTV). The N values indicated the sample size used in the CTV analysis.

2.2.4. Experimental set-up

The elution of the magnetic particles from the QMS separator following pulse injections was studied using the experimental set-up shown diagrammatically in Fig. 3. The fractional flow-rates $Q_{a'}$, $Q_{b'}$, Q_a, and Q_b were controlled using two multi-syringe pumps, one set to injection ($Q_{a'}$, $Q_{b'}$), the other to aspiration (Q_b) mode, such that $Q_{a'} + Q_{b'} = Q_a + Q_b$ (Type 33 syringe pump; Harvard Instruments, Natick, MA, USA). The volumes of the syringes used for pumping the carrier fluid were: $Q_{a'}$, 30 ml; $Q_{b'}$, 140 ml; Q_b, 140 ml (Becton-Dickinson, Franklin Lakes, NJ, USA). The outlet a was left open to the atmosphere to equilibrate the pressure. PTFE tubing of internal diameter of 0.8 mm was used for fluid connections. A six-way valve with a 50-μl sample loop was used for pulse injection of the magnetic particle suspensions (Rheodyne 7725i; Alltech Associates, Deerfield, IL, USA). The outlets a and b of the QMS separator were connected to two on-line UV detectors as described earlier.

The separation element of the QMS separator consisted of two concentric cylinders (the inside cylinder was solid) surrounded by four pole pieces generating the magnetic quadrupole field, as illustrated in Figs. 2 and 3. The QMS inlets and outlets were connected to the QMS separation element by suitable flow manifolds, equipped with the inlet and outlet flow splitters, respectively, Fig. 3. There were two different QMS magnets used in this study, differing in the maximum magnetic field, B_0, and the mean force field strength, S_m, as shown in Table 2. The source of the magnetomotive force were eight 2×2×1 in. bricks of NdFeB permanent magnets (1 in. = 2.54 cm). The quadrupole magnet's aperture, its length, and the dimensions of the flow channels are shown in Table 2. The details of the magnetic field

Table 2
The magnet, the channel and the total flow parameters of the quadrupole magnetic flow sorter (QMS) system[a]

$B_0 = 0.775$ T, mean $S_m = 0.803 \cdot 10^8$ T A/m^2			$B_0 = 1.334$ T, mean $S_m = 2.382 \cdot 10^8$ T A/m^2		
Bead A (ml/min)	Bead B (ml/min)	Bead C (ml/min)	Bead A (ml/min)	Bead B (ml/min)	Bead C (ml/min)
2	3	0.5	5	3	0.5
5	4	1	8	5	1
10	5	2	10	6	2
15	6	3	15	8	3
20	8	5	20	10	5
25	10	8	25	15	8
30	15	10	30	20	10
40	20	15	35	30	15
50			40		
55					
60					

[a] The two quadrupole magnets used in this study differed in the maximum field, B_0, and force field strength, S_m, as shown above, and in the maximum energy product of the permanent magnet elements, 32 and 40 mega-gauss-oersted (MGOe), respectively (Dexter Magnetics, Toledo, OH, USA). The magnets' bore radii were 4.85 mm and 4.82, correspondingly; their length was 76.2 mm. The pole pieces were either designed and manufactured in the laboratory ($B_0 = 0.775$ T) or sub-contracted (Dexter Magnetics); the pole piece material was 1018 cold-rolled low carbon steel. The geometry of the separation channel (designated Mark III) was determined by the inner rod radius, $r_i = 4.76$ mm, and the channel thickness, $h = 2.153$ mm. The inlet flow splitter radius was $r_{s\ in} = 3.124$ mm, the outlet flow splitter radius was $r_{s\ out} = 3.543$ mm. The material of the channel was stainless steel alloy 304. The ratio of the fractional flow-rates was kept constant, $Q_{a'}/Q = 0.1$ and $Q_a/Q = 0.2$, corresponding to $r_{ISC} = 2.842$ mm and $r_{OSC} = 3.035$ mm, respectively. The transport lamina thickness was $r_{OSC} - r_{ISC} = 0.193$ mm. The dead volume of the flow channel (including the inlet and outlet flow manifolds) was 6.3 ml; that of the QMS separation element was 3.56 ml.

geometry inside the separation element of the QMS channel were published elsewhere [12].

Prior to the magnetic particle suspension injection, the system was filled with the degassed carrier solution, with the particular attention paid to the removal of air bubbles from the QMS separator and the fluid lines. Both the inlet and the outlet flow pumps were started and allowed to run for few minutes in order to stabilize the flow distribution inside the separator channel. The total and partial flow-rates used in the study are indicated in Table 2. A 50-µl bolus of the magnetic particle suspension, at a number concentration of approximately $5 \cdot 10^8$/ml, was injected into the valve loop. The injection time was marked through an electrical connection between the valve and the data acquisition board. The development of the elution profiles from the outlets a and b was monitored on the personal computer screen in order to determine the point of return of the detector signal to baseline. The injections were repeated (for each flow-rate setting) once the detector signal returned to baseline (indicating that all particles were cleared from the QMS separator).

Those elution profiles with obvious operator or equipment errors were deleted from further analysis. The magnetic particle distribution between the outlets a, b, and the outer wall, w, was calculated from the elution profiles as described above.

3. Results and discussion

The mathematical model predicted that once under the influence of the magnetic field inside the QMS separation element, the magnetic particles start moving radially, toward the wall of the outer cylinder, Fig. 2. The radial migration velocity, u_m, was directly proportional to the particle magnetophoretic mobility, m, and the magnetic force field strength, S_m, Eq. (13), a constant characteristic of the QMS separation element. The combination of the radial (magnetic) and axial (convective) velocity components determined the position of the particle in the fluid stream when it reaches the outlet flow splitter, and therefore it determined whether or not the particle was eluted at the outlet b. The numerical

simulations of the magnetic particle distributions between the outlets a and b were conducted for all three samples of the magnetic beads, A, B, and C, Table 1, and Fig. 4, for a range of total flow-rates, and for set values of the fractional flow-rates, $Q_{a'}$, $Q_{b'}$, Q_a, and Q_b, Table 2. Inspection of Table 2 and Fig. 4 also shows the mean and standard deviations of the particle magnetic mobilities.

Numerical simulations revealed that the distribution in the magnetophoretic mobility contributed to the spatial distribution of the microbead trajectories in the QMS separation element, and therefore contributed to their relative recoveries in outlets a and b, F_a and F_b, Eq. (6) (Fig. 5). The results of numerical simulations, Fig. 6a, are compared with the experimental results, Fig. 6b. The calculated F_b values showed a characteristic maximum for each magnetic bead type, Fig. 6a. Inspection of the calculated
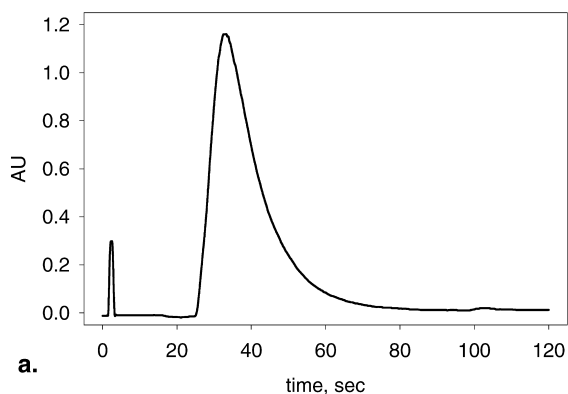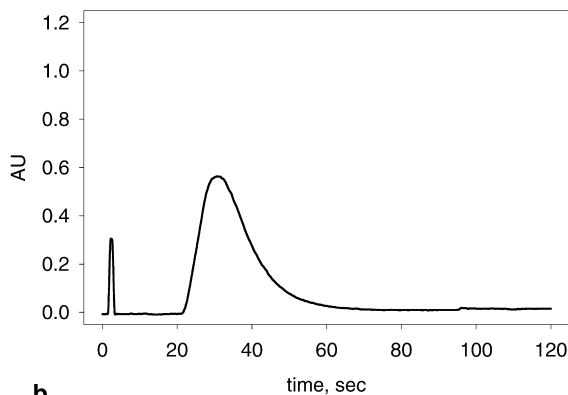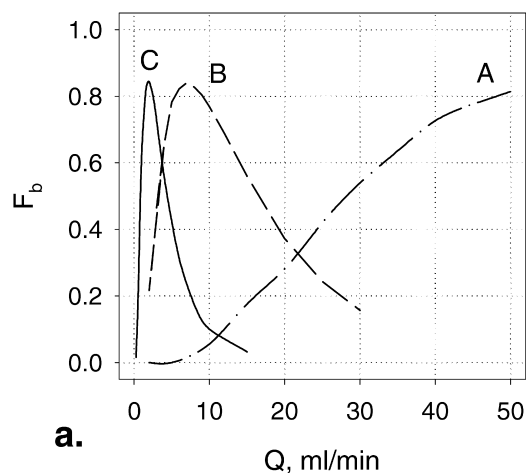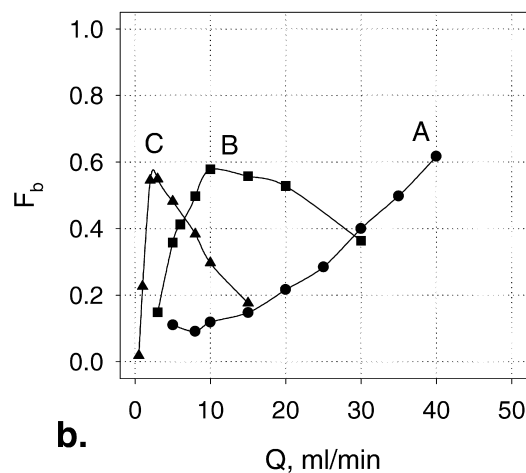

Fig. 5. Representative examples of the magnetic bead elution profiles from the QMS separator. (a) Outlet a. (b) Outlet b.

Fig. 6. The fractional recovery at outlet b as a function of the total flow-rate, Q, for three types of the magnetic beads, A, B and C, and the magnet $B_0 = 1.334$ T. (a) Theory. (b) Experiment.

trajectories inside the QMS sorting element (not shown) revealed that the position of the maximum F_b value depended on certain characteristic mobility values of the sample. At a low total flow-rate a large part of the trajectories corresponding to high mobility particles (above a certain high cut-off mobility, m_3) ended on the wall of the outside cylinder and were not eluted from the QMS separator, with the resulting low value of F_b. With an increasing flow-rate and a resulting decrease in the exposure to the magnetic field, an increasing number of the particle trajectories were directed to the outlet b, with the

corresponding increase in F_b. At the intermediate flow-rate range, most of the particle trajectories traversed the transport lamina, Fig. 2b, without being captured on the outside wall, with the resulting high values of F_b, Fig. 6a. Further increase of the total flow-rate resulted in increasing losses of the low mobility fraction to the outlet a (below a certain low cut-off mobility, m_0) due to the particle inability to cross the transport lamina during a short residence time in the magnetic field.

In summary, numerical simulations of the sorting process predicted the existence of a window of magnetic mobilities, $m_3 - m_0$, for the particle retrieval in outlet b. The association of the maximum particle recovery in outlet b with a certain particle mobility window, $m_3 - m_0$, and its dependence on the total flow-rate was typical of a transport-mode separation process, and the time-of-flight analytical processes [1,7,9,11,13]. The results of the numerical simulations were in agreement with the earlier analysis of the dependence of the QMS sorter throughput on the particle magnetic susceptibility [11].

We observed a remarkable agreement between theory and experiment with respect to the position of the F_b maxima on the Q axis, but not with respect to their values, compare Fig. 6a and b. We also have seen a satisfactory correlation with respect to other system parameters, such as the maximum magnetic field intensity, B_0, and the average magnetophoretic mobility of the microsphere sample, Figs. 6–8.

The experimentally measured retrieval factor, F_b, changed with Q as predicted by the theory, Fig. 6b. The positions of the F_b maxima for bead C were: theory, 2.0 ml/min, experiment, 2.5 ml/min, and for bead B: theory, 7.0 ml/min, experiment, 10.0 ml/min. The upward shift of the peak position with the change in the bead type is explained by the higher saturation magnetization of bead B as compared to bead C, Table 1, with the resulting higher mobility of bead B in the magnetic field. Due to the experimental constraints (limited capacity of the syringes mounted on the syringe pumps) we were not able to reach the maximum retrieval for the highest mobility bead A, Fig. 6b. A high total flow-rate, Q, through the sorter resulted in a high sorting throughput (at constant inlet and outlet fractional flow-rate ratios), which is desirable for high volume operations. Our experimental results confirmed a positive correlation between the particle magnetophoretic mobility and the sorting throughput, as predicted by the theory [11].

We saw evidence of the dependence of the F_b peak position on the strength of the magnetic force. There was an upward shift in the position of the F_b maximum along the Q axis with the increase in the magnetic field, in agreement with the theoretical predictions, Figs. 7 and 8. The effect of the magnetic field was well pronounced for the intermediate-mobility bead type B, compare Figs. 7c and 8c: theory, 4.0 ml/min, experiment, 6.0 ml/min, at low field $B_0 = 0.775$ T; and theory, 7.0 ml/min, experiment, 10.0 ml/min, at high field $B_0 = 1.334$ T. The increase in the magnetic field was too small to detect a significant effect on the weakly magnetic beads, type C, compare Figs. 7a and 8a, for which the theoretical and the experimental F_b maxima clustered between $Q = 1.25$ and 2.5 ml/min. We saw an indication of the shift in the F_b peak position for the most magnetic bead, type A, compare Figs. 7e and 8e, but were unable to confirm it due to the experimental system limitations (limited syringe capacities). The experimental curve for the weaker field, Fig. 7e, had a point of inflection at $Q = 25$ ml/min and appeared to be reaching a maximum at 50 ml/min; the experimental curve for the stronger field, Fig. 8e, did not reach a point of inflection even at $Q = 40$ ml/min, and was steadily rising at that point. Overall, the experiment confirmed the positive correlation between the field and the position of the maximum F_b on the Q axis, and thus the throughput, as predicted by the theory [11].

The highly predictable variations of the experimental F_b peak position with the selected system parameters indicated to us the soundness of the basic assumptions underlying the theory. The significant differences between the predicted and the measured peak heights exposed the weaknesses of the model in describing the finer aspects of the particle motion in the magnetic and flow fields, and the limitations of the experimental design. The experimental values of F_a and F_b did not add up to a value predicted by the theory, Fig. 7b, d and f and Fig. 8b, d and f. The higher than predicted particle losses when the column was placed inside the magnetic field indicated particle retardation at the wall of the outside cylinder
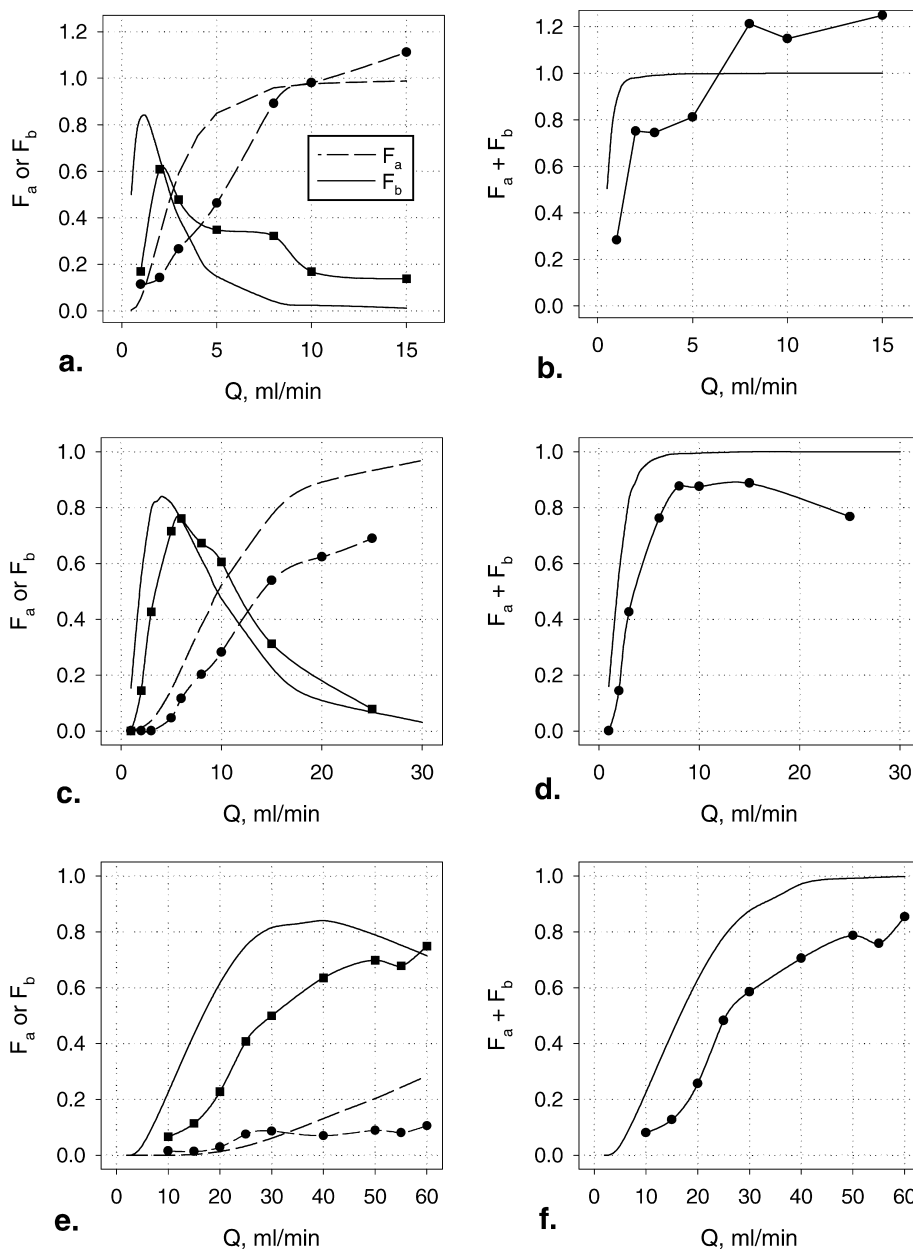
Fig. 7. The fractional recovery at outlets a and b, as a function of the total flow-rate, Q, magnet $B_0 = 0.775$ T. (a, b) Bead C. (c, d) Bead B. (e, f) Bead A.

due to mechanisms which were not accounted for by the theory. Such mechanisms could include the retardation of the particle on the wall due to rolling and mechanical entrapment. Where the theory predicted a plateau with F_a and F_b adding to unity, the

experimental values were not better than 0.8 to 0.9. There could have been experimental limitations which led to lower F_a and F_b values than those predicted by the theory, such as particle losses in the QMS dead spaces (which accounted for over 40% of
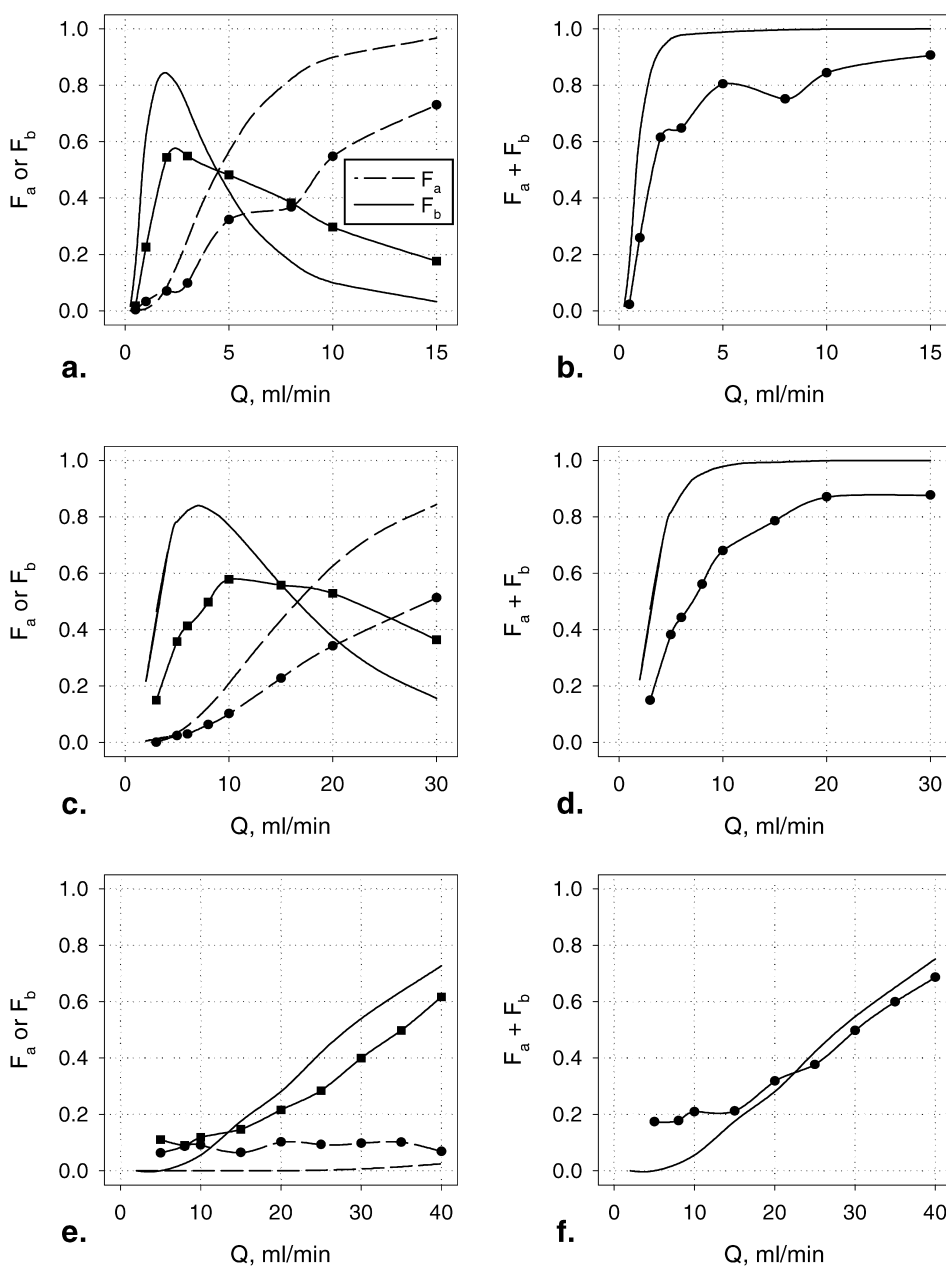
Fig. 8. The fractional recovery at outlets a and b, as a function of the total flow-rate, Q, magnet $B_0 = 1.334$ T. (a, b) Bead C. (c, d) Bead B. (e, f) Bead A.

the total channel volume, Table 2), or the operator error in selecting the time point (t_1) of the elution profile return to baseline, Eq. (18). The mechanisms not included in the model, which could explain the lower than unity total particle recovery are the steric

effects and the lubrication effects. Both effects would contribute to the particle retardation at the accumulation wall. The steric effects would increase the particle losses in the vicinity of the wall due to the particle finite size, leading to an earlier contact

with the wall than if the particle were treated as a point mass. The lubrication effect increases the pressure in the narrow confines between the particle and the wall surfaces relative to the bulk pressure, for particles close to the wall, resulting in hindered particle movement toward the wall. The channel imperfections, particularly the finite thickness of the flow splitters, may have also played a role in the observed deviations from the theory.

There was a consistent pattern of overestimating the F_b values at low flow-rates, Q, and underestimating them at the high flow-rates by the theory, for all three bead types, and two different field intensities, Fig. 7a, c and e and Fig. 8a, c and e. Also, in most cases, the F_a values were lower than those predicted by the theory. There is a tantalizing possibility that these differences were the result of secondary effects characteristic of the particle motion in the viscous fluid. Such effects are usually too weak to be observed directly, and we have omitted them in our theoretical model. The secondary effects arise from including the second- and higher-order terms in the Navier–Stokes equation of the bead motion in the viscous fluid [21,22]. Their manifestations are lift forces in a parabolic flow profile, particularly in the vicinity of solid walls, and lubrication effects in the vicinity of the solid wall. The lift forces come into play with rapid changes in the flow velocity with position, characteristic of high flow-rates through narrow channels (within the laminar flow regime). A possible explanation of the observed differences between the theoretical and experimental values of F_a and F_b is the shift of the particle population from outlet a to outlet b due to lift forces pushing the particles away from the core rod and towards the annular channel center. Even if the effect is small, it could result in the shift of the initial radial position of the particles entering the magnetic field towards the OSC, which, when averaged over many particles, would lead to a noticeable increase in the bead count in the outlet b, with the simultaneous decrease in the bead count in the outlet a, as observed. The shift between the observed and the predicted values of F_a and F_b is particularly pronounced at high flow-rates, which provides additional support to the notion of the fluid-mechanical origin of the observed effect. Characteristically, the

sum of the observed values of F_a and F_b values became closer to 1 at high flow-rates (Fig. 7b and d and Fig. 8d and f) indicating a possible lift force effect in keeping the beads away from the accumulation wall as well. The action of lift forces in the rectangular SPLITT channels has been studied before [7].

It should be emphasized that the theoretical treatment of the separation process did not admit any free variables which would require fitting to the separation experiment results and, in this sense, it provided us with an a priori model of the separation process. The correct prediction by the model of the F_b maxima positions convinced us of the utility of the model in analyzing the fate of the individual particles inside the QMS separation element, and of the usefulness of the SPLITT conceptual framework in analyzing the separation data. The model allowed us to formulate hypotheses explaining the discrepancy between the predicted and the measured heights of the F_b peaks, and to design further experiments for testing such hypotheses. The understanding of the behavior of the magnetic particles in the QMS separator permits us a rational design of the sorter application to biological cell separation.

4. Nomenclature

A	Light absorbance
A_1, A_2	Geometrical constants of the QMS flow channel
B	Magnetic field (field intensity, or field induction, or field flux density)
B_0	Magnetic field at the inner wall of the outer cylinder
c	Number concentration
f_m	Magnetic body force, or Kelvin magnetization force density, Eq. (8)
F_a, F_b, F_w	Retrieval factor in channel a, channel b, Eq. (15), or the accumulation wall, Eq. (20), respectively
FFF	Field-flow fractionation
h	Area under the elution curve $A = A(t)$, or height of the flow channel
H	Magnetic field strength

k	Beer–Lambert law proportionality constant
L	Length of the magnet
m	Magnetophoretic mobility
M	Magnetization
M_s	Saturation magnetization
m_0	Low cut-off mobility (all particles with $m < m_0$ are eluted in outlet a), Fig. 2b
m_3	High cut-off mobility (all particles with $m_3 < m$ are retarded on the channel wall), Fig. 2b
n	Particle number in volume V
N_a, N_b	Total number of particles crossing the detector a or detector b, respectively
$Q = Q_{a'} + Q_{b'}$ $= Q_a + Q_b$	Total flow-rate
$Q_{a'}$	Inlet flow-rate (sample)
$Q_{b'}$	Inlet flow-rate (carrier fluid)
Q_a	Outlet flow-rate (depleted fraction)
Q_b	Outlet flow-rate (enriched fraction)
QMS	Quadrupole magnetic SPLITT fractionator
r	Radial coordinate
r_o	Inner wall of the outer cylinder radius
r_i	Inner wall of the inner cylinder radius
r_s	Flow splitter radius
r_{ISC}	Inlet splitting cylinder radius
r_{OSC}	Outer splitting cylinder radius
r_1	Initial particle position when entering the force field
S_m	Magnetic force field strength (a gradient of the magnetic energy density), Eq. (14)
SPLITT	Split-flow thin fractionation
t_f	Time of the particle flight in the force field
u_m	Radial particle velocity component
v	Axial flow velocity component
$\langle v \rangle$	Average flow velocity in the force field
V	Volume
w	Rectangular channel thickness
$w_{a'}$	ISP distance from the proximal rectangular channel wall (relative to the direction of the force field)
w_a	OSP distance from the proximal rectangular channel wall (relative to the direction of the force field)
z	Axial coordinate
Subscripts	
a	QMS outlet port designation
b	QMS outlet port designation
a′	QMS inlet port designation
b′	QMS inlet port designation
ISC	Inlet splitting cylinder
ISP	Inlet splitting plane
OSC	Outlet splitting cylinder
OSP	Outlet splitting plane
Greek letters	
χ	Magnetic volumetric susceptibility
ρ	$= r/r_o$
μ_0	Magnetic permeability of vacuum

Acknowledgements

References

[1] M. Martin, P.S. Williams, in: F. Dondi, G. Guichon (Eds.), Theoretical Advancements in Chromatography and Related Separation Sciences, Vol. 383, Kluwer, Dordrecht, 1992, p. 513.

[2] J.C. Giddings, Sep. Sci. Technol. 20 (1985) 749.

[3] G.H. Batchelor, in: An Introduction to Fluid Dynamics, Cambridge University Press, Cambridge, 1994, p. 222.

[4] C. Bor Fuh, S. Levin, J.C. Giddings, Anal. Biochem. 208 (1993) 80.

[5] G.H. Markx, R. Pethig, Biotech. Bioeng. 45 (1995) 337.

[6] P.R.C. Gascoyne, X. Wang, J. Yang, J. Vykoukal, F.F. Becker, in: 8th International Symposium on Field-Flow Fractionation, Paris, 6–8 September 1999, Abstract L13.

[7] P.S. Williams, Sep. Sci. Technol. 29 (1994) 11.

[8] S. Levin, Israel J. Chem. 30 (1990) 257.

[9] M. Zborowski, P.S. Williams, L. Sun, L.R. Moore, J.J. Chalmers, J. Liq. Chromatogr. Rel. Techn. 20 (1997) 2887.

[10] L. Sun, M. Zborowski, L.R. Moore, J.J. Chalmers, Cytometry 33 (1998) 469.

[11] P.S. Williams, M. Zborowski, J.J. Chalmers, Anal. Chem. 71 (1999) 3799.

[12] M. Zborowski, L. Sun, L.R. Moore, P.S. Williams, J.J. Chalmers, J. Magnetism Magn. Mater. 194 (1999) 224.

[13] P.H. Dawson, in: P.H. Dawson (Ed.), Quadrupole Mass Spectrometry, Elsevier, New York, 1976, p. 9.

[14] J.J. Chalmers, M. Zborowski, L. Sun, L.R. Moore, Biotechnol. Prog. 14 (1998) 141.

[15] P.S. Williams, S. Levin, T. Lenczycki, J.C. Giddings, Ind. Eng. Res. 31 (1992) 2172.

[16] V. Tchikov, A. Kuznetsov, A. Shapiro, S. Winoto-Morbach, W. Mueller-Ruchholtz, J. Magnetism Magn. Mater. 122 (1993) 367.

[17] J.J. Chalmers, Y. Zhao, M. Nakamura, K. Melnik, L. Lasky, L.R. Moore, M. Zborowski, J. Magnetism Magn. Mater. 194 (1999) 231.

[18] L.R. Moore, M. Zborowski, M. Nakamura, K. McCloskey, S. Gura, M. Zuberi, S. Margel, J.J. Chalmers, J. Biochem. Biophys. Methods 44 (2000) 115.

[19] P. Reschiglian, D. Melucci, G. Torsi, Chromatographia 44 (1997) 172.

[20] S. Margel, S. Gura, H. Bamnolker, B. Nitzan, T. Tennenbaum, B. Bar-Toov, H. Hinz, H. Seliger, in: U. Hafeli, W. Schuett, W. Teller, M. Zborowski (Eds.), Scientific and Clinical Applications of Magnetic Carrieres, Plenum Press, New York, 1997, p. 37.

[21] J. Happel, H. Brenner, in: Low Reynolds Number Hydrodynamics, Prentice-Hall, Englewood Cliffs, NJ, 1965, p. 286.

[22] C. Pozrikidis, Boundary Integral and Singularity Methods for Linearized Viscous Flow, Cambridge University Press, Cambridge, 1992.